

Microstructural contributions to hole transport in *p*-type GaN:Mg

A. K. Rice and K. J. Malloy^{a)}

Center For High Technology Materials, University of New Mexico, Albuquerque, New Mexico 87106

(Received 19 January 2000; accepted for publication 24 October 2000)

We present an analysis of hole transport in *p*-type Mg-doped GaN grown on sapphire substrates by metalorganic chemical vapor deposition. We find that the experimental Hall mobility cannot be described by numerically solving the Boltzmann transport equation. We attribute this discrepancy to the microstructure of GaN:Mg grown on sapphire and present a microstructure-oriented model of the transport of holes in *p*-type GaN:Mg grown on sapphire. This model provides a simplified picture of the microstructure consisting of two distinct microstructural phases in GaN on sapphire. Using this model for the experimental mobility, the extracted parameters from hole transport measurements suggest a weak direct correlation with the microstructural parameters determined from x-ray diffraction measurements. The experimental mobility of *p*-type GaN:Mg grown on sapphire can be described as dependent upon the acceptor doping, impurity compensation, and microstructure, including dislocation density, columnar grain size, and grain boundaries. © 2001 American Institute of Physics. [DOI: 10.1063/1.1334375]

I. INTRODUCTION

The transport characteristics of *p*-type Mg-doped GaN have generated much interest in recent years since the achievement of *p*-type GaN.¹ Concerns followed, with the realization that *p*-type GaN:Mg possesses a high resistivity due to compensation, a hole activation energy of 150–200 meV, and a low hole mobility.^{2–7} Furthermore, the microstructure of GaN:Mg grown on sapphire is inhomogeneous and can be characterized as an ordered polycrystal,^{8,9} where individual grains are of high crystalline quality but are tilted and twisted with respect to one another.

This article presents an analysis of the Hall mobility for GaN:Mg, as thus far, a complete understanding of transport in *p*-type GaN:Mg is lacking. Such an analysis can be a powerful means of characterizing semiconductor transport, yielding information about the impurity concentration, impurity compensation, carrier scattering mechanisms, material parameters, and in this case, film microstructure. This analysis includes calculation of the mobility of crystalline GaN:Mg by numerically solving the Boltzmann transport equation (BTE). A numerical calculation of the BTE is necessary to accurately account for the inelastic scattering mechanisms dominant at high temperature. All major scattering processes, screening, and wave-function overlap have been incorporated.

It is found that unlike the hole mobility in other III–V compound semiconductors, the experimental hole mobility of GaN:Mg is not well described by extended state scattering mechanisms. Differences between the calculated and experimental Hall mobilities are observed throughout the entire temperature range investigated. However, this study will focus on the discrepancies observed at high temperature where optical phonon scattering is dominant. The final interpretation of the behavior of the Hall mobility in GaN:Mg includes

the effects of an inhomogeneous microstructure. The influence of the microstructure on the electrical properties of GaN:Mg qualitatively explains the discrepancies between the experimental Hall mobility and the calculated crystalline mobility of GaN:Mg.

In support of this approach, the GaN:Mg microstructure is examined by high resolution x-ray diffraction (XRD) and atomic force microscopy (AFM), and a correlation required by our model between the film structure and the mobility is observed. Finally, with improvement in the growth of GaN:Mg, hole transport will approach single crystalline GaN:Mg. Hence, the calculated limits of pure crystalline *p*-type GaN:Mg conductivity and mobility are presented.

II. TRANSPORT CALCULATION

Transport theory in compound semiconductors assumes the validity of the effective mass approximation, Bloch wave functions, perturbation theory, and the Boltzmann transport equation. In this study, the hole mobility for crystalline GaN:Mg was calculated by iteratively solving the BTE following Nag's procedure,¹⁰ providing an accurate calculation for both low and high temperatures. The mobility calculation explicitly takes into account carrier screening and overlapping wave functions, and includes ionized impurity, nonpolar acoustic phonon (deformation potential), piezoelectric, nonpolar optical phonon, and polar optical phonon scattering mechanisms. Each scattering mechanism exhibits a characteristic temperature dependence and by analyzing the temperature dependence of the carrier mobility, the relative importance of each mechanism is obtained. Furthermore, by comparing calculated and experimental mobilities, the contributions of each scattering mechanism to the mobility are determined. However, in order to calculate the mobility due to various scattering mechanisms it is necessary to use reasonable physical parameters for GaN:Mg. Hence, Sec. II A addresses the material parameters used in the transport study.

^{a)}Author to whom correspondence should be addressed; electronic mail: malloy@chtm.unm.edu

TABLE I. Material parameters used for calculating the mobility of *p*-type GaN:Mg.

Heavy hole effective mass	m_h^*	$1.89m_0^a$
Light hole effective mass	m_l^*	$0.337m_0^a$
Split-off effective mass	m_{so}^*	$0.813m_0^a$
Light hole energy	E_{lh} (meV)	6^{a-e}
Split-off hole energy	E_{so} (meV)	24^{a-e}
Low frequency dielectric constant	ϵ_s	9.5^f
High frequency dielectric constant	ϵ_0	5.35^f
Longitudinal polar optical temperature	Θ (K)	1055^{f-h}
Nonpolar acoustical deformation potential	E_{NPA} (eV)	1^i
Nonpolar optical deformation potential	E_{NPO} (eV)	2^j
Piezoelectric constant	h_{14} (C m ⁻²)	0.5^k
Mass density	ρ (10 ³ kg m ⁻³)	6.10^l
Acoustical velocity	s (10 ³ m s ⁻¹)	6.59^g

^aReference 11.

^bReference 12.

^cReference 13.

^dReference 14.

^eReference 15.

^fReference 16.

^gReference 17.

^hReference 18.

ⁱReference 19.

^jThe optical deformation potential is assumed to be approximately twice the value of the acoustic deformation potential following Wiley (Ref. 20). Most III-V *p*-type semiconductors have $E_{npo}/E_{npa} \sim 2$.

^kReference 21.

^lReference 22.

A. Material parameters

The material parameters used in this calculation are summarized in Table I. While there are many uncertainties about the valence band structure of wurtzite GaN, theoretical calculations in conjunction with experiments have provided estimates for various properties of the valence band. The parameters necessary for performing the transport calculations include hole effective masses, Γ point valence band energies, dielectric constants, optical phonon energy, scattering potentials, piezoelectric constants, the mass density, and the acoustical velocity.

Transverse and longitudinal effective masses for the heavy hole (HH) band, light hole (LH) band, and split off (SO) band of GaN have been estimated in theoretical band calculations.¹¹ Subsequently, the effective masses for the HH, LH, and SO bands are obtained from $m^* = (m_{\perp}^2 m_{\parallel})^{1/3}$, giving $m_{HH}^* = 1.89m_0$, $m_{LH}^* = 0.337m_0$, and $m_{SO}^* = 0.813m_0$, where m_0 is the electronic mass. In addition, theoretical band calculations¹¹ along with experimental data¹²⁻¹⁵ have predicted that the valence band for *p*-type GaN consists of three nondegenerate bands. The Γ point energies employed were an average of the following (taking the heavy hole valence band as 0 meV): $E_{LH} = 5.84$ meV,¹¹ 6 meV,¹²⁻¹⁵ and $E_{SO} = 26.1$ meV,¹¹ 22 meV,¹⁴ 28 meV,¹³ 18 meV,¹² 24 meV,¹⁵ yielding $E_{LH} = 6$ meV and $E_{SO} = 24$ meV. Moreover, the density of states effective mass for the valence band is defined as

$$m_h^{*3/2} = m_{HH}^{*3/2} + m_{LH}^{*3/2} \exp\left(\frac{-E_{LH}}{k_b T}\right) + m_{SO}^{*3/2} \exp\left(\frac{-E_{SO}}{k_b T}\right),$$

giving at 300 K $m_h^* \approx 2m_0$. The low and high frequency

dielectric constants were taken as 9.5 and 5.35,¹⁶ respectively. Since the longitudinal optical phonon energy has been reported as 90 meV,¹⁷ 91.2 meV,¹⁸ and 92 meV,¹⁶ an average value of 91 meV was employed, yielding a longitudinal polar optical temperature of $\hbar\omega/k_b = \theta = 1055$ K. However, current uncertainties in the valence band structure are such that the scattering potentials in *p*-type GaN are not accurately known. Kim *et al.*¹⁹ have calculated the acoustic deformation potential to be 0.8 eV with an uncertainty of at least 2 eV. Hence, a value of 1 eV has been adopted for the acoustic deformation potential E_{npa} . Furthermore, the optical deformation potential E_{npo} for most III-V compound semiconductors is approximately a factor of 2 larger than the acoustic deformation potential.²⁰ Thus 2 eV has been used for the optical deformation potential. The piezoelectric constant h_{pz} or e_{14} has been estimated from data on *n*-type GaN mobility²¹ as 0.375 C m⁻² and from electromechanical coupling coefficients of *n*-type GaN (Ref. 21) as 0.6 C m⁻². Hence, a value of $h_{pz} = 0.5$ C m⁻² has been adopted. The lattice mass density was taken as $\rho = 6.1 \times 10^3$ kg m⁻³.²² Finally, the acoustic velocity s was calculated from the estimated longitudinal elastic constant¹⁷ c_l , where $c_l = \rho s^2$. The estimated longitudinal constant is $c_l = 26.53 \times 10^{10}$ N m⁻², yielding $s = 6.59 \times 10^3$ m s⁻¹.

Given that the valence band structure for wurtzite GaN is only spin degenerate¹¹ at $k=0$, transport only in the HH band has been considered. The possible error introduced by this assumption is analyzed as follows. The concentration in the LH or SO band is less than 5%–15% of the free hole concentration in the temperature range studied. Comparing the HH, LH, and SO effective mass and assuming the scattering rate is the same as for the HH band, the mobility for the LH band and SO band are estimated at $6\mu_{HH}$ and $2\mu_{HH}$, respectively, where μ_{HH} is the mobility in the heavy hole band. If parallel band conduction were considered, the Hall mobility would be given by

$$\mu_H = \frac{p_{LH}\mu_{LH}^2 + p_{HH}\mu_{HH}^2 + p_{SO}\mu_{SO}^2}{p_{LH}\mu_{LH} + p_{HH}\mu_{HH} + p_{SO}\mu_{SO}}, \quad (1)$$

where μ_{LH} and μ_{SO} represent the light hole and split off hole mobility and p_{HH} , p_{LH} , and p_{SO} denote the heavy hole, light hole, and split off hole carrier concentration, respectively. At high temperature where $p_{HH} \sim 0.8p$, $p_{LH} \sim 0.05p$, and $p_{SO} \sim 0.15p$, the net effect of Eq. (2.1) is to increase the modeled mobility by approximately twice the HH band mobility. Thus, transport in the parallel band will increase the calculated mobility as compared to only HH band transport. However, scattering among the HH, LH, and SO bands also needs to be included and will reduce the mobility. Full treatment of multiband hole transport is left for future studies and only transport in the HH band is considered here.

III. TEMPERATURE DEPENDENT HALL MEASUREMENTS

A. Experimental details

The samples investigated were grown on sapphire substrates by metalorganic chemical vapor deposition. Samples I, III, and IV were grown in the same laboratory A, while

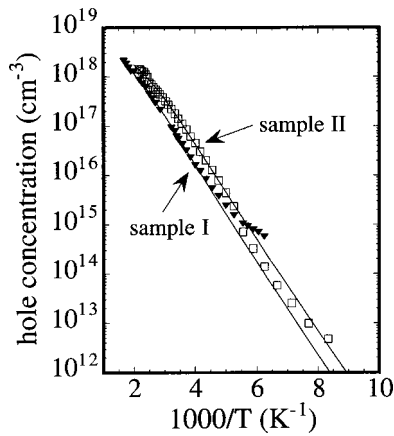


FIG. 1. Hall hole concentration as a function of inverse temperature for *p*-GaN. Solid triangles and open squares represent experimental data for samples I and II, respectively. Solid lines result from least-squares fits of the charge balance equation to the experimental data.

sample II was grown in a different laboratory B. Ammonia (NH₃), trimethyl gallium, and bis-cyclopentadienyl (BCP-Mg) were used as a source of nitrogen, gallium, and magnesium. For the samples grown in laboratory A the GaN films were grown on *c*-plane sapphire with a low temperature (480–495 °C) buffer layer approximately 200 Å thick. Two epitaxial GaN layers, grown at temperatures between 900 and 915 °C, were undoped and doped *p* type, respectively, by varying the BCP-Mg flow rate. The undoped layer, approximately 0.5–1 μm thick, was grown with a BCP-Mg flow rate of 30 sccm. A BCP-Mg flow rate of 90 sccm was used for the *p*-type epitaxial layer having a thickness of 2–2.5 μm. Similar growth conditions apply for sample II. The total thickness of each sample as determined from ellipsometry is 2.8, 2.8, 2.9, and 3.5 μm for samples I, II, III, and IV, respectively. Ohmic contacts were formed by annealing a Pt/Au metallization at 750 °C in flowing N₂ for 10 min.²³ This anneal also served to activate the GaN:Mg. Hall effect measurements were performed using a Hall bar to obtain the sheet resistivity, sheet carrier concentration, and mobility as a function of temperature between 120 and 500 K. Repeatable Hall measurements were obtained only after allowing the temperature to stabilize for 5 min and averaging 100 data points. The minimum temperature at which Hall measurements could be performed was determined by the voltage compliance of the Hall current source.

B. Carrier concentration analysis of experimental Hall data

The temperature dependence of the hole concentration for samples I and II is shown in Fig. 1. For each sample the

value of the acceptor concentration N_A , compensation ratio $K=N_D/N_A$, and activation energy E_a , were determined by performing a least-squares fit to the experimental Hall hole concentration p as a function of temperature. An equation giving the free hole concentration was found by applying Boltzmann statistics and charge neutrality yielding

$$p + N_D^+ = \frac{N_A}{\frac{g_0}{g_1} \exp\left(\frac{E_A - E_F}{k_b T}\right) + 1}, \quad (2)$$

where $g_0=2$ and $g_1=1$ are the degeneracies of the unoccupied and occupied acceptor states, respectively.

The values of N_A , K , and E_a , obtained by fitting the charge balance equation to the hole concentration data as a function of temperature for the samples, are given in Table II. Also included in Table II are the room temperature mobility and carrier concentration. In addition, samples I, II, and III were investigated by secondary-ion-mass spectroscopy. The results reveal a physical acceptor concentration of approximately 10^{20} cm^{-3} for each sample. The difference between the physical magnesium concentration 10^{20} cm^{-3} and the acceptor concentration determined from Hall measurements, given in Table II, implies that not all magnesium is electrically active on substitutional lattice sites.

For reasons due to the effect of the microstructure on transport properties that will be discussed in Sec. V, it was not possible to derive a consistent fit for ionized impurity concentrations from both the carrier concentration and the mobility data as is the usual practice in other III–V compound semiconductors.

C. Mobility analysis of experimental Hall data

The calculated lattice-limited mobility for single crystal GaN:Mg as a function of temperature is shown in Fig. 2. Polar optical phonon, nonpolar optical phonon, piezoelectric, and nonpolar acoustical phonon scattering mechanisms have been included. Due to the polar nature of GaN,²⁴ piezoelectric and polar optic scattering mechanisms are dominant at low and high temperatures, respectively. Furthermore, this lattice limited mobility curve sets an upper mobility limit for single crystal GaN:Mg.

Figures 3(a) and 3(b) display the hole mobility of GaN:Mg as a function of temperature for samples III and II, respectively. Shown are the calculated mobility curve, the combined lattice scattering curve, the ionized impurity scattering curve, and the experimental data. The two dominant scattering mechanisms for impure crystalline GaN:Mg are ionized impurity scattering at low temperatures and polar optical scattering at high temperatures. Two observations can

TABLE II. Impurity concentrations, compensation ratio, activation energy, 300 K free hole concentration, and 300 K mobility for each sample investigated.

Sample	N_A (10^{18} cm^{-3})	N_D (10^{18} cm^{-3})	K	E_a (meV)	p (10^{17} cm^{-3})	μ ($\text{cm}^2 \text{ V}^{-1} \text{ s}^{-1}$)
I	14	8.2	0.58	153	0.7	6.2
II	9.6	1.5	0.15	173	2.03	15.2
III	2.4	0.7	0.3	183	0.8	7.7
IV	7.0	3.3	0.48	148	1.0	15.9

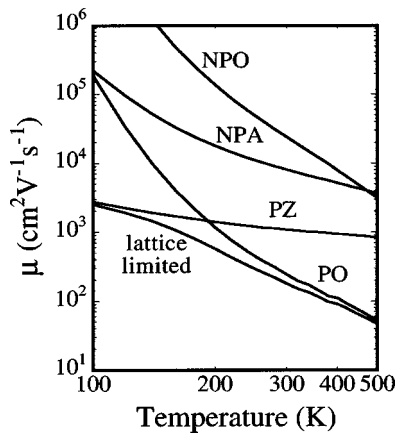
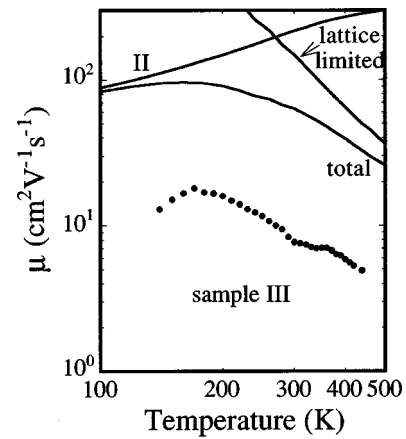


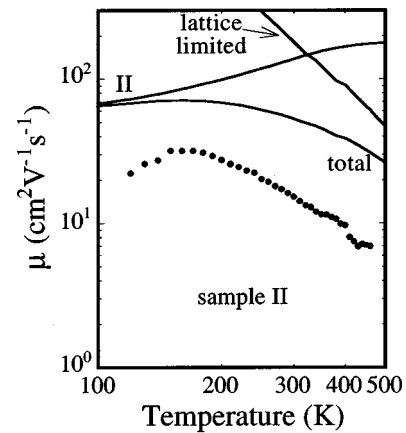
FIG. 2. Individual hole lattice scattering mechanisms for *p*-type GaN:Mg: (a) PO: polar optical phonon, (b) NPO: nonpolar optical phonon, (c) NPA: nonpolar acoustical phonon, (d) PZ: piezoelectric, (e) lattice limited: combined lattice scattering.

be made from Fig. 3. The calculated mobility is at least a factor of 4 greater than the experimental data for all samples and temperatures, and the experimental data shows different high temperature, lattice-limited mobilities in each sample. Figures 4(a) and 4(b) correspondingly display the experimental hole mobility and the calculated mobility as a function of temperature for each sample studied. Examining Fig. 4, we see that not only are the mobilities not accurately modeled by solving the BTE, but that the calculated results do not properly model the trend in experimental mobility values between samples with different net impurity concentrations. For example, sample II has a higher ionized impurity concentration than sample III, a fact reflected in the BTE calculation giving a lower mobility. However, the experimental results are exactly reversed—the sample with more impurities, sample II, has a higher mobility.

Clearly more factors control transport than have been included in the BTE solution. For example, neutral impurity scattering has been neglected. The two limiting values of neutral impurity scattering have been considered. The highest resulting mobility assumes the number of neutral impurities is determined by the acceptor concentration, while the lower limit assumes the total magnesium concentration acts as neutral impurity scatterers. For instance, using the parameter $N_N = N_A - N_D - p$, as determined from the Hall measurement, inclusion of neutral impurity scattering for sample II reduces the total mobility by at most 15%. However, assuming the density of neutral impurities N_N to be the physical magnesium concentration of approximately 10^{20} cm^{-3} , the mobility is further reduced to a maximum value of $19 \text{ cm}^2 \text{ V}^{-1} \text{ s}^{-1}$, well below the experimental value. Furthermore, this modeled mobility possesses a much weaker temperature dependence than the experimental mobility at both low and high temperature. This modeled mobility is too low, probably because the neutral impurity scattering model assumes isolated and noninteracting neutral impurities, highly unlikely with such a large value of N_N . The actual contribution of neutral impurity scattering probably lies within these two limits.



(a)



(b)

FIG. 3. Calculated and experimental hole mobility as a function of temperature. II: ionized impurity, lattice limited: calculated lattice limited mobility, total: total calculated mobility, solid dots are experimental data: (a) sample I: $N_A = 14 \times 10^{18} \text{ cm}^{-3}$, $K = 0.58$, $E_a = 153 \text{ meV}$; (b) sample II: $N_A = 9.6 \times 10^{18} \text{ cm}^{-3}$, $K = 0.15$, $E_a = 173 \text{ meV}$.

Although some of the material parameters for GaN:Mg are uncertain, these uncertainties are not large enough to account for the discrepancy between the calculated and experimental curves. Piezoelectric and optical polar phonon are the two major lattice scattering mechanisms in *p*-type GaN:Mg. At 100 K, the piezoelectric mobility must be reduced so that the total mobility, including ionized impurity mobility and piezoelectric mobility, fit the experimental mobility. For example, in Fig. 3(b), a 30% increase in the piezoelectric constant to a value of 0.67 C m^{-2} , or a decrease in the acoustic velocity of 25% to a value of $4.93 \times 10^3 \text{ m s}^{-1}$ is required to fit the experimental mobility. This value of $h_{pz} = 0.67 \text{ C m}^{-2}$ is a possible correction for the low temperature discrepancies, however, the discrepancies at high temperature are still unaccounted for.

For high temperature, optical polar phonon scattering is dominant. Polar optical phonon scattering is dependent upon the low and high frequency dielectric constant. At 450 K, a reduction of 360% is required to fit the calculated mobility to the experimental mobility. This requires that $(k_0^{-1} - k_s^{-1})$ increase by 500% to a value of approximately 0.5, from the

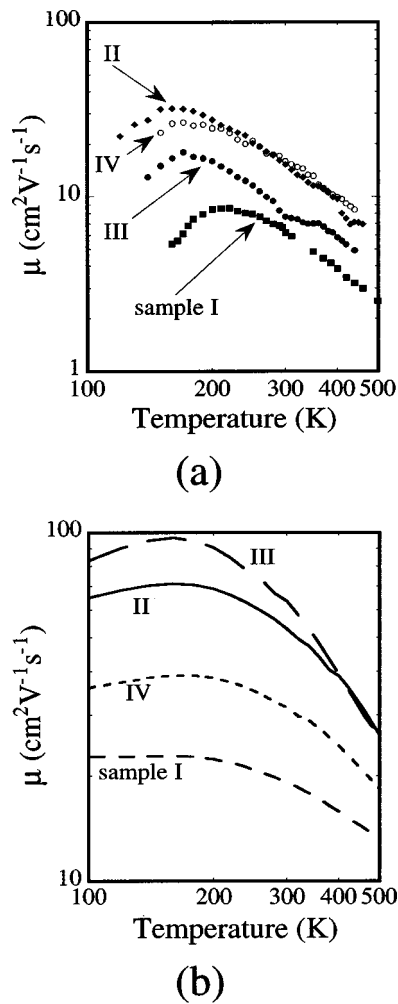


FIG. 4. Hall mobility as a function of temperature for *p*-type GaN:Mg: (a) Experimental data: solid squares, solid diamonds, solid circles, and open circles represent experimental mobility for samples I, II, III, and IV, respectively; (b) mobility calculation for each sample investigated using material parameters given in Tables I and II.

utilized value of 0.0816. As this large a discrepancy in material properties is highly unlikely, our discussion suggests that the deviation in the calculated mobility cannot be solely explained by the uncertainty in the material parameters employed. Furthermore, since material parameters should be constant between samples, only such factors as ionized impurities and crystalline quality (dislocation density, grain boundary area, and grain size) vary between samples. We attribute the mobility discrepancies to the role of these microstructural variations in GaN on sapphire.

IV. DISCUSSION OF FILM STRUCTURE

Upon examining the film surface with AFM, information about the bulk material can be obtained. Figures 5(a) and 5(b) display AFM images of samples II and III, respectively. The white and black regions in the AFM image denote a peak and a valley, respectively. The AFM image shown in Fig. 5(a) reveals “wall-like” growth regions where it appears two columnar grains have coalesced. Furthermore, upon investigating Fig. 5(b) the circled region contains

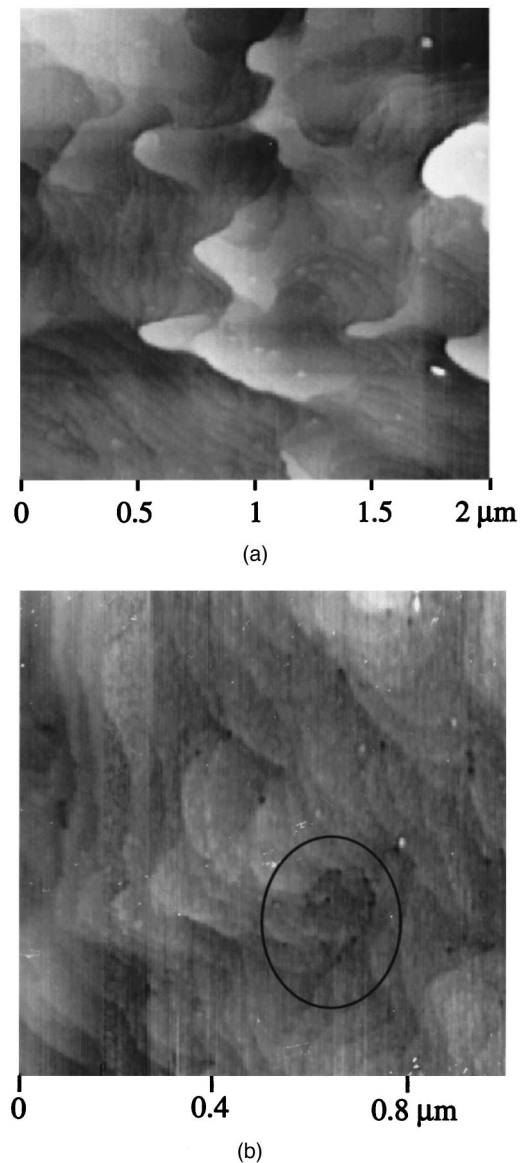


FIG. 5. Atomic force microscopy (AFM) topographs for samples in this study. (a) sample II, (b) sample III. The white and black regions in the AFM image denote a peak and a valley, respectively. The AFM image shown in (a) reveals “wall-like” growth regions where it appears two columnar grains have coalesced. (b) includes a circled region containing black dots that are lined up. They are thought to be dislocations clustered in the grain boundary region mapping out a grain region.

“black dots” that are lined up. These are thought to be dislocations clustered in the grain boundary region mapping out a grain region.²⁵

Transmission electron microscopy studies of *n*-type GaN grown on sapphire²⁶ have shown grain sizes ranging from 50 to 500 nm with dislocations clustered at the low angle grain boundaries. Scanning capacitance microscopy has also revealed possible grain sizes of 1 μm .²⁵ In regions surrounding both pure edge and mixed/screw dislocations, they observed a reduced change in capacitance with applied voltage as compared to “dislocation free” regions. These regions tended to lie along the boundaries formed during the coalescence of GaN islands in the early stages of growth. In addition, cathodoluminescence has revealed a correlation be-

tween grain size and yellow luminescence.⁹ Reference 9 proposed defect states inside grains at the low-angle grain boundaries are the origin of the yellow luminescence. Although these studies have investigated *n*-type GaN, it is reasonable to assume the microstructure of GaN:Mg is also a highly ordered polycrystal containing grain and grain boundary regions. This statement is supported, in part, by the investigation of the GaN:Mg film structure by AFM, as shown in Fig. 5.

Transport studies in *n*-type GaN^{27–30} have alluded to the role of the microstructure on the transport properties. Tang *et al.*²⁷ observed discrepancies in their high temperature *n*-GaN mobility data and corrected their calculated fit with a “crystal defect” scattering mechanism that possessed a $CT^{-1.5}$ temperature dependence, where C is a fitting constant. Furthermore, Look *et al.*³¹ used N_A and $(k_0^{-1} - k_s^{-1})$ as fitting parameters and noticed a 30% discrepancy from the $(k_0^{-1} - k_s^{-1})$ literature value, implying at higher temperatures the calculated fit needed to be reduced by 30%. However, GaN on sapphire typically possesses dislocation densities on the order of $10^8 - 10^{10} \text{ cm}^{-2}$.^{26,32} Therefore dislocation scattering may contribute to the reduction in the experimental mobility, and has been recently examined in *n*-type GaN.^{28–30} Dislocation scattering is usually treated as based either on an electrostatic interaction with carriers³³ or on the strain field interaction with carriers.³⁴ Both scattering mechanisms assume noninteracting dislocations, unlikely in heavily dislocated GaN and contrary to transmission electron microscopy studies of GaN on sapphire.²⁶ More importantly, the temperature coefficients for the electrostatic and strain field scattering mechanisms are both positive (meaning the scattering rate decreases with increasing temperature) and fail to explain the discrepancies observed at high temperature. Thus while it is possible dislocation scattering describes the discrepancies at low temperature,^{28–30} it cannot explain the high temperature differences. Instead, we choose to model the discrepancies between the experimental and calculated Hall mobility as the result of hole transport in two distinct microstructural phases in GaN on sapphire.

V. MICROSTRUCTURAL BASED DISCUSSION OF ELECTRICAL PROPERTIES

To interpret the discrepancies between the experimental and the calculated mobility a microstructure-oriented transport model, similar to one first proposed by Bube,³⁵ has been invoked. This model is attractive because it is the simplest picture that includes transport through two electrically distinct regions as invoked by more complicated models of transport in polycrystalline materials. In general, other models of transport between the grain and grain boundary regions exist and a review is given by Lahiri *et al.*³⁶ However, without any experimental evidence about the electrical properties of grain boundary regions in *p*-type GaN:Mg, we model transport in *p*-type GaN:Mg as simple ohmic conduction through two distinct microstructural phases. The model consists of an inhomogeneous semiconductor possessing single crystal grain regions of dimension l_g , and resistivity ρ_g , separated by disordered grain boundary regions of dimension l_{gb} and resistivity ρ_{gb} , as illustrated in Fig. 6(a).

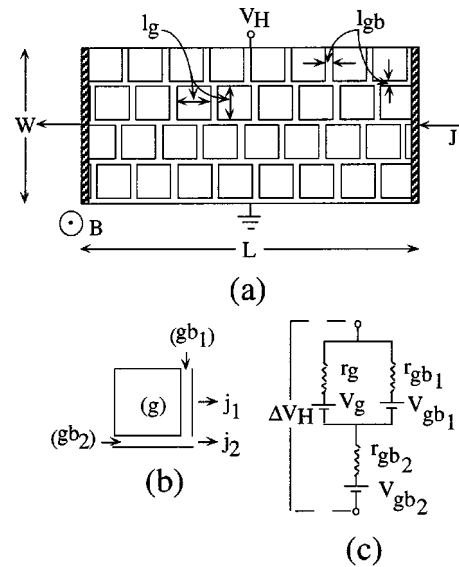


FIG. 6. (a) Schematic representation of Bube’s model with grains of dimensions l_g separated by grain boundaries of dimensions l_{gb} . (b) Basic unit of a grain showing bulk (g) and boundary (gb) regions. (c) Equivalent circuit to describe the Hall voltage. V_H and ΔV_H are the Hall voltage, j_1 and j_2 are the current density for the two current pathways in the basic unit, and r_g , r_{gb1} , r_{gb2} , V_g , V_{gb1} , and V_{gb2} are the resistance and voltage drop across the grain (g) and grain boundary (gb) regions used to calculate the Hall voltage.

The apparent resistivity and the apparent Hall voltage are calculated and the Hall constant, free carrier density, and the Hall mobility are subsequently derived. The conductivity of an inhomogeneous material as shown in Fig. 6(a) supports two parallel current paths. One path traverses the grain boundary region while the second path travels through the grain and the grain boundary region in series. Based on the theory just described the general equation for the measured resistivity is given by

$$\rho = \frac{(1 + \beta)(\rho_g + \rho_{gb}\beta)}{1 + \beta + \alpha\beta + \beta^2}, \tag{3}$$

where $\beta = l_{gb}/l_g$ and $\alpha = \rho_g/\rho_{gb}$.

The inhomogeneous transport model, as shown in Fig. 6(a), simply reduces to transport in one element, as shown in Fig. 6(b). Subsequently, the Hall voltage was treated as a series-parallel assemblage of the basic unit as indicated in Fig. 6(b). Using the equivalent circuit, shown in Fig. 6(c), an expression for the Hall voltage ΔV_H is ascertained. The measured Hall constant R is related to ΔV_H by $R = \Delta V_H / JB(l_g + l_{gb})$, where J is the total current density and B is the applied magnetic field. The apparent carrier density p_{app} and the Hall mobility μ_{app} are calculated from the Hall constant R via $p = (Rq)^{-1}$ and $\mu = R/\rho$. For $\alpha, \beta \ll 1$, it can be shown that the measured free carrier concentration can be expressed as

$$p_{app} = \frac{p_g}{1 + \beta(1 + \beta/\alpha)}, \tag{4}$$

and the apparent Hall mobility as

$$\mu_{app} = \mu_g \frac{\alpha}{\alpha + \beta} + \beta \mu_{gb}. \tag{5}$$

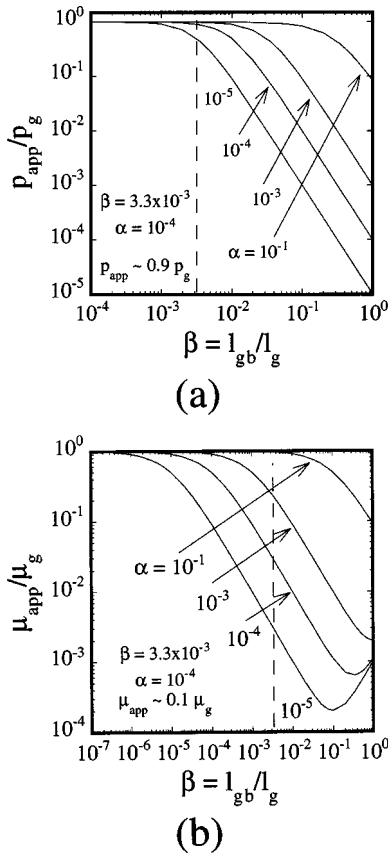


FIG. 7. (a) The apparent carrier concentration divided by the grain carrier concentration ratio plotted as a function of $\beta = l_{gb}/l_g$ for various values of $\alpha = p_g/p_{gb}$. (b) The apparent mobility divided by the grain mobility ratio plotted as a function of $\beta = l_{gb}/l_g$ for various values of $\alpha = p_g/p_{gb}$. For typical values of β and α the inhomogeneity influences the mobility measurement more than the carrier concentration Hall measurement.

Figures 7(a) and 7(b) display the apparent free carrier concentration and the apparent Hall mobility as a function of β for various α values. As will be shown later in the section, typical values of β and α are approximately 10^{-3} and 10^{-4} , respectively. Hence, from Eq. (4) and Fig. 7(a), the apparent carrier density is principally determined by the grain carrier density. Thus, the experimentally measured values for N_A , K , and E_a change little upon including the effects of inhomogeneity. However, from Eq. (5) and Fig. 7(b) the apparent Hall mobility is greatly influenced by the sample inhomogeneity, for example $\mu_{app} \sim 0.1 \mu_g$ for $\alpha = 10^{-4}$ and $\beta = 10^{-3}$. Hence, the sample inhomogeneity prevents a consistent fit of the ionized impurity concentration from both the carrier concentration and the mobility data.

Recall $\beta = l_{gb}/l_g$ is a constant but $\alpha = p_g/p_{gb} = \mu_{gb}p_{gb}/\mu_g p_g$ will vary with temperature. Thus, the apparent Hall mobility will depend upon β , p_{gb}/p_g and μ_{gb}/μ_g . The grain region is assumed single crystal GaN, thus, the grain region material parameters p_g and μ_g are known from our previous mobility calculations given in Sec. III C. The inhomogeneous material has been modeled as crystalline particles separated by disordered interparticle regions. Thus, this simple ohmic conduction model essentially consists of an assemblage of series and parallel temperature dependent resistors.

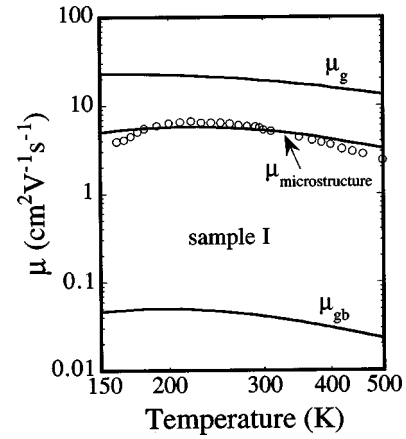


FIG. 8. Mobility as a function of temperature. Shown are the grain (crystalline) mobility, grain boundary mobility, experimental mobility for sample I, and least squares fit of the experimental data to the apparent mobility, given in Eq. (2.5), from the microstructure-oriented model.

Instead of fitting the p_g/p_{gb} ratio directly, this ratio can be assumed to result from a potential barrier or step (positive or negative) V_B at the grain boundary. Hence, the equation used to model the hole concentration in the grain boundary region is $p_{gb} = p_g \exp(-qV_B/k_bT)$, where q , k_b , and T represent the electronic charge, Boltzmann constant, and temperature, respectively. Regardless of any functional relationship describing p_g/p_{gb} , our model simply fits the p_g/p_{gb} ratio.

A least squares nonlinear fit of Eq. (5) to the temperature dependent experimental Hall mobility for each sample was performed. The fitting parameters were β , V_B , A , and B , where A and B are related to the apparent grain boundary mobility by $\mu_{gb} = (AT^{1.5} + BT^{-1.5})^{-1}$. This equation used to model the grain boundary mobility is a traditional mobility equation using Matthiessen's rule to add the mobility assuming two scattering mechanisms, ionized impurity scattering, and polar optical phonon lattice scattering. This initial assumption was again used due to the lack of information known about the grain boundary region. Figure 8 displays the results of the least squares fit for sample I. Shown are mobility curves for crystalline GaN:Mg (in the grain region), the experimental data, the grain boundary region, and the microstructure-oriented model. Figure 8 illustrates the reduction in modeled mobility owing to an inhomogeneous material. The extracted parameters, β^{-1} , V_B , A , and B are displayed in Table III.

The best fit to the experimental mobility data requires that the apparent grain boundary mobility be on the order of $0.01 \text{ cm}^2/\text{V s}$ and possess a slight temperature dependence. Furthermore, as stated previously, dislocation scattering may influence the mobility at low temperature, as shown by n -type GaN.³⁰ Our model accounts for dislocation scattering indirectly in the temperature dependence of the grain boundary mobility. For the samples investigated the values of V_B correspond to room temperature p_g/p_{gb} ratios of 0.5 to 1.

While the discrepancies between experimental mobility and the modeled mobility are probably due to a combination of factors, the average grain-to-grain boundary size ratio of the material, as determined from transport, is one parameter that can be independently verified. Therefore, in support of

TABLE III. Parameters extracted from the microstructure-oriented model and the Williamson–Hall plot. They include β^{-1} , the grain-to-grain boundary length ratio A and B , coefficients of the apparent grain boundary mobility V_B , the extracted barrier height, and L_{\parallel} , α_{tilt} , which, respectively, denote the average lateral coherence length and angle of tilt each grain possesses.

Sample	$\beta^{-1} = l_g / l_{gb}$	A (V s cm ⁻² K ^{-3/2})	B (V s cm ⁻² K ^{3/2})	V_B (mV)	L_{\parallel} (nm)	α_{tilt} (deg)
I	207	3.4×10^{-3}	2.4×10^4	0.6	594	0.15
II	351	3.4×10^{-3}	1.3×10^4	-8.7	835	0.06
III	223	4.4×10^{-3}	1.7×10^4	-5.4	219	0.11
IV	311	3.8×10^{-3}	2.3×10^4	-19.8	331	0.13

this inhomogeneous transport model, the GaN:Mg film microstructure was characterized by XRD.

VI. XRD ANALYSIS

High-resolution x-ray rocking curves were performed using a triple axis diffractometer with an analyzer crystal. In this configuration, the resolution limit of the instrument is 13 arc sec. The lateral coherence length and amount of tilt each columnar grain possesses is determined from the investigation of (00l) symmetric (ω -scan) rocking curve full width at half maximum (FWHM).

A. Analysis of the symmetric rocking curve

For the resolution limits stated above, the symmetric (00l) rocking curve (ω -scan) breadth is controlled only by the out-of-plane misorientation or tilt α_{tilt} and by the lateral coherence length L_{\parallel} parallel to the sample surface. The contributions from each of these broadening mechanisms can be determined by following a procedure similar to Williamson and Hall.³⁷ Here, $\beta_{\Omega}(\sin \theta) / \lambda$ is plotted against $(\sin \theta) / \lambda$, where β_{Ω} is the integral width of the ω scan, λ is the x-ray wavelength, and 2θ is the scattering angle. A similar analysis of the defect structure has been performed on n-type GaN.³⁸

The Williamson–Hall plot separates the tilt and lateral coherence contributions to the peak breadth. The broadening in reciprocal space due to tilt will increase with scattering order, while the breadth due to the presence of a lateral coherence length is independent of the distance from the k -space origin. Subsequently, from the y intersection y_0 and slope m of a linear fit to the $\beta_{\Omega}(\sin \theta) / \lambda$ versus $(\sin \theta) / \lambda$ plot, the correlation length $L_{\parallel} = 0.9 / (2y_0)$ and the tilt angle $\alpha_{\text{tilt}} = m$ are estimated. Figure 9 displays the Williamson–Hall plot for the (00l) rocking curve FWHM for each sample

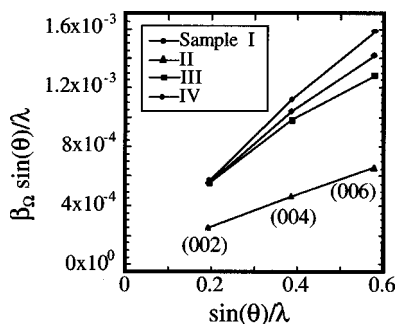


FIG. 9. Williamson–Hall plot of the rocking curve FWHM of symmetric XRD peaks.

investigated. The lateral correlation lengths and the tilt angles are provided in Table III. As shown, sample II possesses columnar grains with larger in-plane coherence lengths and a tilt, with respect to the c axis, smaller by half than the three other samples.

VII. CORRELATION BETWEEN XRD AND MICROSTRUCTURE-ORIENTED MODEL COHERENCE LENGTH

A weak direct correlation (with a correlation coefficient of 0.48) between the lateral correlation length L_{\parallel} , as determined from x-ray diffraction, and the extracted ratio $\beta^{-1} = l_g / l_{gb}$, as determined from the inhomogeneous transport model, has been observed.³⁹ The weak direct correlation between L_{\parallel} and β^{-1} is shown in Fig. 10. The straight line represents a best linear fit to the data. The less than perfect correlation may be due in part to the following reasons. Clearly more factors control transport than have been included. For example, the transport may depend upon the different degrees of twist or tilt between adjoining grains, and each sample realistically possesses a different range of grain sizes. However, only an average size was estimated. Furthermore, the effects of many factors giving rise to the discrepancies between the experimental and modeled mobility have been reduced to one parameter β^{-1} , the grain-to-grain-boundary length ratio. In addition β^{-1} , a ratio, was compared to a physical length L_{\parallel} . Ideally, one would like to correlate the grain size l_g , as determined from transport, to the lateral coherence length L_{\parallel} , as determined from XRD. However, no independent information about the grain

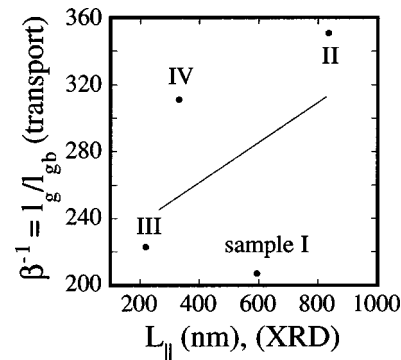


FIG. 10. Shown is the extracted ratio of grain-to-grain boundary length $\beta^{-1} = l_g / l_{gb}$, as determined from the microstructure-oriented model as a function of L_{\parallel} , as determined from XRD. The straight line represents a best linear fit to the data.

boundary exists. Thus, the less than ideal correlation between L_{\parallel} and β^{-1} can manifest itself in the difference in l_{gb} for each sample. Accepting the fact that a small sample set has been studied, these results suggest that there may be a correlation between the microstructure and the transport properties of p -type GaN:Mg, warranting a more extensive study.

In addition, experimental mobility is not correlated with the lateral coherence length L_{\parallel} . This is understandable since the experimental mobility is also dependent upon the acceptor concentration, impurity compensation, and the microstructure. For example, just as the mobility of p -type GaN:Mg grown on sapphire cannot be modeled by only considering the traditional extended state scattering mechanisms, the mobility cannot be modeled by only considering the material quality.

In summary, it has been shown that the experimental mobility of GaN:Mg appears to be influenced by the microstructure. A model has been provided to explain the high temperature discrepancies between the mobility numerically calculated to accurately account for the inelastic scattering of polar optic phonons and the experimental mobility. Furthermore, a direct, but weak, correlation required by the inhomogeneous model between the lateral correlation length, as determined by XRD, and the extracted ratio $\beta^{-1} = l_g / l_{gb}$ was observed.

VIII. CONDUCTIVITY AND MOBILITY LIMITS IN SINGLE CRYSTAL GaN:Mg

Eventually, with improved growth of GaN, the material will approach ideal single crystal quality. Such an improved quality might be expected for the “lateral epitaxial overgrowth” material now being investigated in several laboratories^{40–44} or other novel growth techniques.⁴⁵ In these cases the mobility of p -type GaN:Mg should be well described by traditional extended state scattering mechanisms. Figures 11(a) and 11(b) display the calculated mobility and conductivity for crystalline p -type GaN:Mg with an activation energy of 150 meV and compensation ratio of $K=0.1$ as a function of Mg doping concentration. As shown, the conductivity has an upper limit of $10 (\Omega \text{ cm})^{-1}$ at 300 K and $30 (\Omega \text{ cm})^{-1}$ at 500 K. Subsequently, as the growth of p -type GaN:Mg improves, GaN devices that include p -type GaN:Mg will still possess a high spreading resistance.

IX. SUMMARY

From the analysis of the p -type GaN:Mg Hall mobility, it has been shown that the experimental Hall mobility cannot be explained solely by traditional extended state scattering mechanisms. We see not only that the mobilities are not accurately modeled by solving the BTE, but that the calculated results do not even reflect the trend in experimental mobility values between samples. For instance, sample II has a higher ionized impurity concentration than sample III, a fact reflected in the BTE calculation giving a lower mobility. However, the experimental results are exactly reversed—the sample with more impurities, sample II, has a higher mobility. We attribute these discrepancies to the role of the micro-

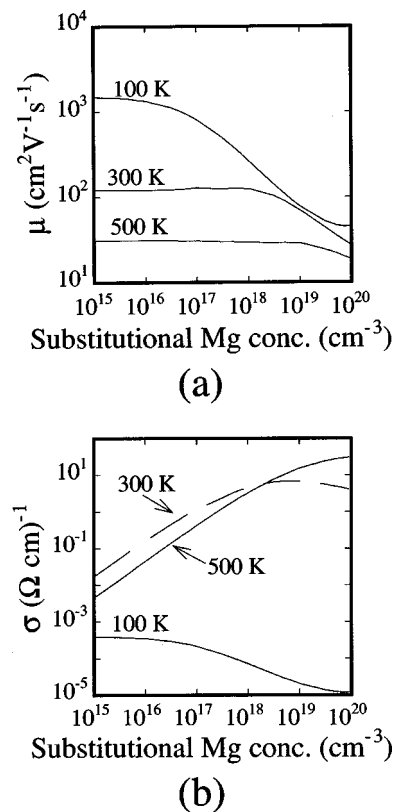


FIG. 11. (a) Calculated low-field hole mobility for p -type GaN:Mg as a function of the Mg concentration for ambient temperatures of 100, 300, and 500 K. (b) Calculated conductivity for p -type GaN:Mg as a function of Mg doping concentration for ambient temperatures of 100 K (solid), 300 K (dashed), and 500 K (solid). For compensation, $K=0.1$ and $E_a = 150$ meV.

structure. While dislocation scattering may control the low temperature mobility it does not explain the discrepancies observed for high temperature. A microstructure-oriented model is presented for an interpretation of the transport of holes in p -type GaN:Mg grown on sapphire. The microstructure-oriented model provides a simplified picture of the microstructure, consisting of two distinct microstructural phases in GaN on sapphire. Using this model for the experimental mobility, a correlation coefficient of 0.48 was found between the microstructural parameters extracted from hole transport measurements and the microstructural parameters determined from XRD measurements. This result is suggestive that there may be a correlation between the microstructure and the transport properties of p -type GaN:Mg warranting a more extensive study. Therefore, the experimental mobility of p -type GaN:Mg grown on sapphire is properly described as dependent upon the acceptor doping, impurity compensation, and microstructure, including dislocation density, columnar grain size, and grain boundaries.

¹H. Amano, M. Kito, K. Hiramatsu, and I. Akasaki, Jpn. J. Appl. Phys., Part 2, **28**, L2112 (1989).

²W. Götz, N. M. Johnson, J. Walker, D. P. Bour, and R. A. Street, Appl. Phys. Lett. **68**, 667 (1996).

³W. Götz, N. M. Johnson, J. Walker, D. P. Bour, H. Amano, and I. Akasaki, Appl. Phys. Lett. **67**, 2666 (1995).

⁴T. Tanaka, A. Watanabe, H. Amano, Y. Kobayashi, I. Akasaki, S. Yamazaki, and M. Koike, Appl. Phys. Lett. **65**, 593 (1994).

- ⁵H. Nakayama, P. Hacke, M. R. H. Kahn, T. Detchprohm, K. Hiramatsu, and N. Sawaki, *Jpn. J. Appl. Phys., Part 2* **35**, L282 (1996).
- ⁶L. Sugiura, M. Suzuki, and J. Nishio, *Appl. Phys. Lett.* **72**, 1748 (1998).
- ⁷S. Fujita, M. Funato, D.-C. Park, Y. Ikenaga, and S. Fujita, *MRS Internet J. Nitride Semicond. Res.* **4S1**, G6.31 (1999).
- ⁸S. D. Hersee, J. C. Ramer, and K. J. Malloy, *MRS Bull.* **22**, 45 (1997).
- ⁹F. A. Ponce, D. P. Bour, and W. Götz, *Appl. Phys. Lett.* **68**, 57 (1996).
- ¹⁰B. R. Nag, *Electron Transport in Compound Semiconductors*, 1st ed. (Springer, New York, 1980), Vol. 11.
- ¹¹Y. C. Yeo, T. C. Chong, and M. F. Li, *J. Appl. Phys.* **83**, 1429 (1997).
- ¹²R. Dingle, D. D. Sell, S. E. Stokowski, and M. Ilegems, *Phys. Rev. B* **4**, 1211 (1971).
- ¹³B. Monemar, *Phys. Rev. B* **10**, 676 (1974).
- ¹⁴D. Volm *et al.*, *Phys. Rev. B* **53**, 16543 (1996).
- ¹⁵K. Pakula *et al.*, *Solid State Commun.* **97**, 919 (1996).
- ¹⁶A. S. Barker and M. Ilegems, *Phys. Rev. B* **7**, 743 (1973).
- ¹⁷D. L. Rode, in *Semiconductors and Semimetals Transport Phenomena*, edited by A. C. Beer and R. K. Willardson (Academic, New York, 1975), Vol. 10, pp. 1–89.
- ¹⁸V. W. Chin, T. L. Tansley, and T. Osotchan, *J. Appl. Phys.* **75**, 7365 (1994).
- ¹⁹K. Kim, W. R. L. Lambrecht, and B. Segall, *Phys. Rev. B* **53**, 16310 (1996).
- ²⁰J. D. Wiley, in *Semiconductors and Semimetals; Vol. 10*, edited by R. K. Willardson and A. C. Beer (Academic, New York, 1975), pp. 91–174.
- ²¹A. D. Bykhovski, V. V. Kaminski, M. S. Shur, Q. C. Chen, and M. A. Kahn, *Appl. Phys. Lett.* **68**, 818 (1996).
- ²²Landolt-Börstein, *Semiconductors, Group IV Elements and III-V Compounds* (Springer, New York, 1980), Vol. III/17a.
- ²³D. J. King, L. Zhang, J. C. Ramer, S. D. Hersee, and L. F. Lester, *Mater. Res. Soc. Symp. Proc.* **468**, 421 (1997).
- ²⁴W. A. Harrison, *Electronic Structure and the Properties of Solids—The Physics of the Chemical Bond* (Dover, New York, 1989).
- ²⁵P. J. Hansen *et al.*, *Appl. Phys. Lett.* **72**, 2247 (1998).
- ²⁶W. Qian, M. Skowronski, M. De Graef, K. Doverspike, L. B. Rowland, and D. K. Gaskill, *Appl. Phys. Lett.* **66**, 1252 (1995).
- ²⁷H. Tang, W. Kim, A. Botchkarev, G. Popovici, F. Hamdani, and H. Morkoç, *Solid-State Electron.* **42**, 839 (1998).
- ²⁸N. G. Weimann, L. F. Eastman, D. Doppalapudi, H. M. Ng, and T. D. Moustakas, *J. Appl. Phys.* **83**, 3656 (1998).
- ²⁹H. M. Hg, D. Doppalapudi, T. D. Moustakas, N. G. Weimann, and L. F. Eastman, *Appl. Phys. Lett.* **73**, 821 (1998).
- ³⁰D. C. Look and J. R. Sizelove, *Phys. Rev. Lett.* **82**, 1237 (1999).
- ³¹D. C. Look, J. R. Sizelove, S. Keller, Y. F. Wu, U. K. Mishra, and S. P. DenBaars, *Solid State Commun.* **102**, 297 (1997).
- ³²R. C. Powell, N.-E. Lee, Y.-W. Kim, and J. E. Green, *J. Appl. Phys.* **73**, 189 (1993).
- ³³B. Pödör, *Phys. Status Solidi* **16**, K167 (1966).
- ³⁴D. L. Dexter and F. Seitz, *Phys. Rev.* **96**, 964 (1952).
- ³⁵R. H. Bube, *Appl. Phys. Lett.* **13**, 136 (1968).
- ³⁶S. K. Lahiri, S. Das, B. Umapathi, and S. Kal, *IETE J. Res.* **43**, 193 (1997).
- ³⁷G. K. Williamson and W. H. Hall, *Acta Metall.* **1**, 22 (1953).
- ³⁸T. Metzger *et al.*, *Philos. Mag. A* **77**, 1013 (1998).
- ³⁹The correlation coefficient represents to what degree one random variable affects another random variable. The correlation will vary between -1 and 1 . A correlation coefficient of 1 indicates a direct linear relationship between two variables, while a coefficient of -1 indicates an indirect (anti-correlated) relationship between two variables. A coefficient equal to zero implies the two variables are independent.
- ⁴⁰T. S. Zheleva, O.-H. Nam, M. Bremser, and R. F. Davis, *Appl. Phys. Lett.* **71**, 2472 (1997).
- ⁴¹O.-H. Nam, M. D. Bremser, T. S. Zheleva, and R. F. Davis, *Appl. Phys. Lett.* **71**, 2638 (1997).
- ⁴²H. Marchand, J. P. Ibbetson, P. T. Fini, P. Kozodoy, S. Keller, S. DenBaars, J. S. Speck, and U. K. Mishra, *MRS Internet J. Nitride Semicond. Res.* **3**, 3 (1998).
- ⁴³H. Marchand, X. H. Wu, J. P. Ibbetson, P. T. Fini, S. Keller, J. S. Speck, S. P. DenBaars, and U. K. Mishra, *Appl. Phys. Lett.* **73**, 747 (1998).
- ⁴⁴T. S. Zheleva, W. M. Ashmawi, O.-H. Nam, and R. F. Davis, *Appl. Phys. Lett.* **74**, 2492 (1999).
- ⁴⁵D. Zubia and S. D. Hersee, *J. Appl. Phys.* **85**, 6492 (1999).